Optics Letters

Heterogeneous integration of Si photodiodes on silicon nitride for near-visible light detection

Stijn Cuyvers,[1,2,*] Artur Hermans,[1,2,3] Max Kiewiet,[1,2] Jeroen Goyvaerts,[1,2] Gunther Roelkens,[1,2] Kasper Van Gasse,[1,2,4] Dries Van Thourhout,[1,2] and Bart Kuyken[1,2]

[1]Photonics Research Group, INTEC Department, Ghent University - imec, 9052 Ghent, Belgium
[2]Center for Nano- and Biophotonics, Ghent University, Belgium
[3]Research Laboratory of Electronics, Massachusetts Institute of Technology, Cambridge, Massachusetts, USA
[4]E. L. Ginzton Laboratory, Stanford University, Stanford, California, USA
*Corresponding author: stijn.cuyvers@ugent.be

Received 3 November 2021; revised 15 December 2021; accepted 11 January 2022; posted 11 January 2022; published 11 February 2022

Silicon nitride (SiN) is used extensively to complement the standard silicon photonics portfolio. However, thus far demonstrated light sources and detectors on SiN have predominantly focused on telecommunication wavelengths. Yet, to unlock the full potential of SiN, integrated photodetectors for wavelengths below 850 nm are essential to serve applications such as biosensing, imaging, and quantum photonics. Here, we report the first, to the best of our knowledge, microtransfer printed Si p–i–n photodiodes on a commercially available SiN platform to target wavelengths <850 nm. A novel heterogeneous integration process flow was developed to offer a high microtransfer printing yield. Moreover, these devices are fabricated with CMOS compatible and wafer-scale technology.

https://doi.org/10.1364/OL.447636

Introduction. Silicon nitride (SiN) has been widely recognized as a promising integrated photonic platform to complement silicon-on-insulator technology [1,2]. The low propagation losses, negligible nonlinear absorption, and wide transparency window have sparked academic and commercial interest in SiN for diverse applications, including telecommunications [3], optical frequency comb generation [4,5], and quantum photonics [6]. In addition, the low index contrast with silicon oxide results in enhanced resilience to fabrication errors and a reduced mode confinement. This has made SiN the material of choice for life-science and biosensing applications at visible wavelengths [7–9]. However, the integration of active devices on SiN has proven challenging. Despite considerable progress with heterogeneous [10–12] and hybrid integration [13], these developments have mostly focused on infrared wavelengths in the telecom range. Demonstrations of light sources and detectors on SiN beyond the classic telecom wavelengths remain scarce, hampering the adoption of SiN photonic integrated circuits (PICs) for several applications.

State-of-the-art photodetectors on SiN have been developed on a variety of material platforms, such as germanium [14], silicon (Si) [15–17], and III–V semiconductors [12,18]. Yet, to the best of our knowledge, very few demonstrations are geared toward detection below 850 nm. An edge-coupled monolithic Si rib avalanche photodetector on SiN for 685 nm was demonstrated in Ref. [16], whereas microtransfer printed grating-assisted GaAs p–i–n photodiodes, targeting wavelengths around 800 nm, were reported in Ref. [12]. Although a low dark current and a high responsivity were reported in the latter, a silicon platform is generally preferred for avalanche gain multiplication [19].

Here, we present, to our knowledge, the first microtransfer printed Si p–i–n photodiodes on SiN for wavelengths below 850 nm. The photodetector is based on a doped silicon rib waveguide and is printed on top of imec's BioPIX plasma-enhanced chemical vapor deposition (PECVD) SiN platform. The low deposition temperature of PECVD SiN ensures full compatibility with complementary metal-oxide semiconductor (CMOS) technology [20]. A new process flow is developed to suspend the Si p–i–n devices on the silicon-on-insulator (SOI) source wafer with a high yield, enabling seamless heterogeneous integration with commercial SiN platforms. Moreover, the devices are fabricated using wafer-scale technology, allowing for low-cost and scalable manufacturing.

Device design and fabrication. The Si p–i–n photodetectors are realized on imec's iSiPP25G integrated silicon photonics platform through a multi-project wafer (MPW) run. Rib waveguides are defined in a 220 nm Si layer on top of a 2 μm thermally grown silicon oxide (SiO_2) layer. The rib has a width of 500 nm and a shallow etch depth of 70 nm. The intrinsic region spans over 1.3 μm, as depicted in Fig. 1. At the sides, 850 nm wide P- and N-doped regions, with a doping concentration of 1.5×10^{18} cm^{-3}, and 4.3 μm wide P^+/N^+ doped regions with a doping concentration of 10^{20} cm^{-3} are created.

The photonic target wafer comprises a SiN PIC based on imec's BioPIX platform. The 300 nm thick SiN layer is deposited by PECVD on top of a 3.3 μm SiO_2-on-Si wafer. Furthermore, a 2 μm deep recess is locally etched in the SiO_2 top cladding using

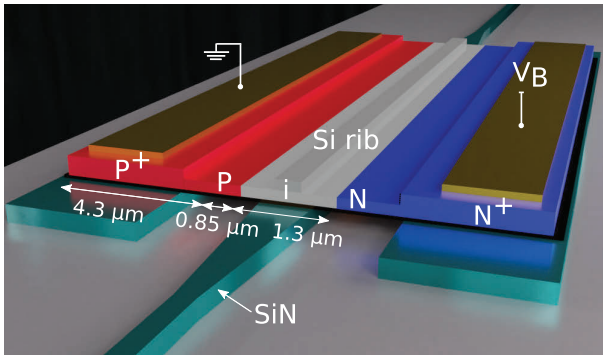

Fig. 1. Rendering of the Si p–i–n photodiode on top of a SiN waveguide. The device is reverse biased by applying a voltage V_B via the metal contacts on top of the doped P^+/N^+ regions.

dry etching techniques to expose part of the SiN waveguide, enabling evanescent coupling to the Si rib waveguide above it.

For the heterogeneous integration of the photodiodes, the microtransfer printing technique is used [5,12]. It relies on the kinetically controlled adhesion of an elastomeric polydimethylsiloxane (PDMS) stamp to pick devices from a source wafer and print them on a target wafer. An important advantage of microtransfer printing is its ability to integrate devices in a recess, an attribute that is essential for compatibility with top-cladded passive photonic platforms. In addition, this integration technique combines several advantages of flip-chip integration and wafer bonding, such as massively parallel integration, efficient usage of the source material, and the possibility of co-integrating different material stacks [5,12].

Before the microtransfer printing process can commence, the photodetectors need to be encapsulated and suspended on the source wafer. As a first step, the sample is submerged in buffered hydrofluoric acid (HF) to remove the SiO_2 cladding on top of the Si device layer [Figs. 2(a) and 2(b)]. Next, a TI-35E photoresist is spincoated and patterned to define the encapsulation tethers [Fig. 2(c)]. To make the photoresist more resilient to the HF release etchant, a hard bake at 145°C is used. The sample is subsequently cooled down at a slow pace of ~10°C/min to avoid cracks in the photoresist. Finally, the sacrificial SiO_2 layer underneath the Si coupons is underetched for 3 h using HF vapor [Fig. 2(d)]. In contrast to liquid HF, vapor-phase HF provides a near 100% picking yield as it does not suffer from capillary forces that can lead to a collapse of the suspended Si device layer. After the release etch, the coupons are solely supported by the encapsulation resist tethers and are ready for microtransfer printing. A micrograph of the suspended 200 µm long Si photodetector is shown in Fig. 3(a).

To ensure a high printing yield, an 80 nm adhesive divinylsiloxane-bis-benzocyclobutene (DVS-BCB) layer is spincoated on the target SiN wafer. The source and target wafer are then loaded in a X-Celeprint µTP-100 microtransfer printing tool, which provides an alignment accuracy of 1.5 µm (3σ). A PDMS stamp with a size of 200 µm × 50 µm was used to pick up and print the photodiode. The microtransfer printing step is illustrated in Figs. 2(e) and 2(f). Pattern recognition markers enable automated alignment of the photodiodes on the target wafer. Furthermore, if wafer-scale fabrication is envisioned, array stamps can be utilized to enable a number of coupons to be picked up and printed simultaneously. After transfer printing, the photoresist encapsulation is removed

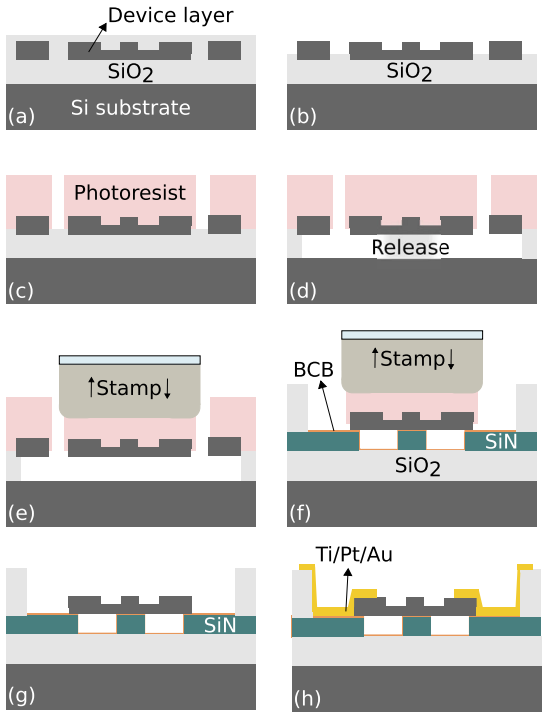

Fig. 2. Device process flow: (a) Si device layer on imec's iSiPP25G platform; (b) top oxide removal using buffered HF; (c) photoresist encapsulation and patterning; (d) vapor-phase HF release etch; (e) pick-up from source wafer; (f) print on SiN target wafer; (g) encapsulation removal; (h) final metallization.

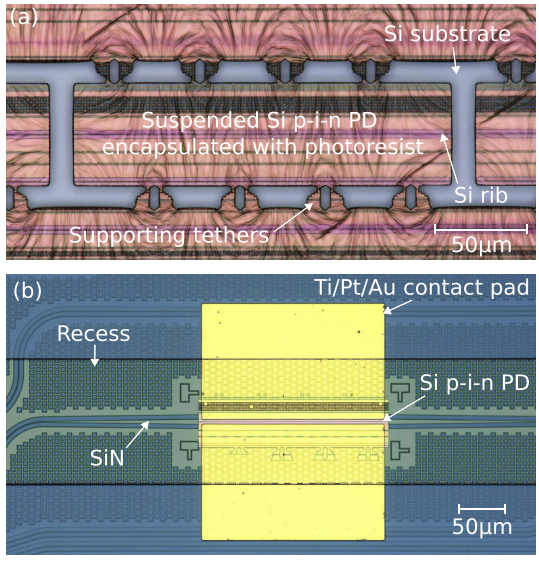

Fig. 3. Micrographs of (a) a suspended photodiode on source wafer and (b) a microtransfer printed and post-processed photodiode on the silicon nitride target wafer.

using an oxygen plasma reactive ion etch (RIE) [Fig. 2(g)]. Thereafter, the sample is baked at 280°C to cure the DVS-BCB layer. Finally, a liftoff process is employed to pattern the Ti/Pt/Au metal contact pads [Fig. 2(h)]. Just prior to the metal deposition, the sample is submerged for 5 s in diluted buffered HF and subsequently for 5 s in H_2SO_4:H_2O_2:H_2O (1:1:40) to

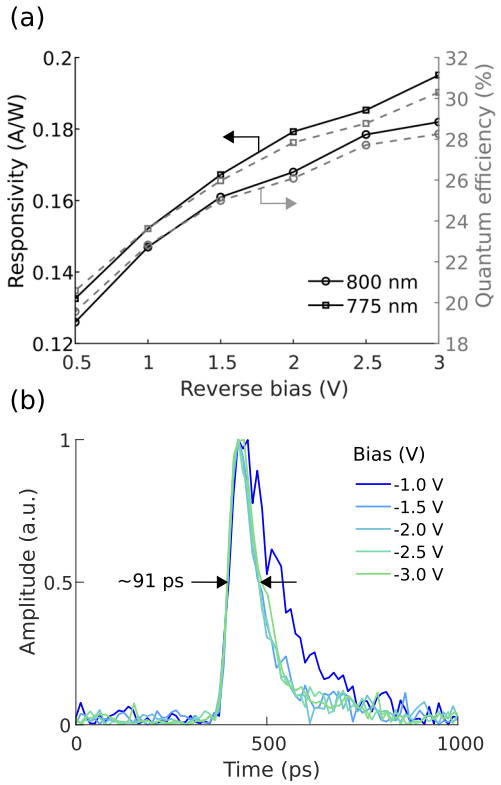

Fig. 4. (a) Measured photodiode responsivity and external quantum efficiency and (b) measured impulse response as a function of reverse bias voltage.

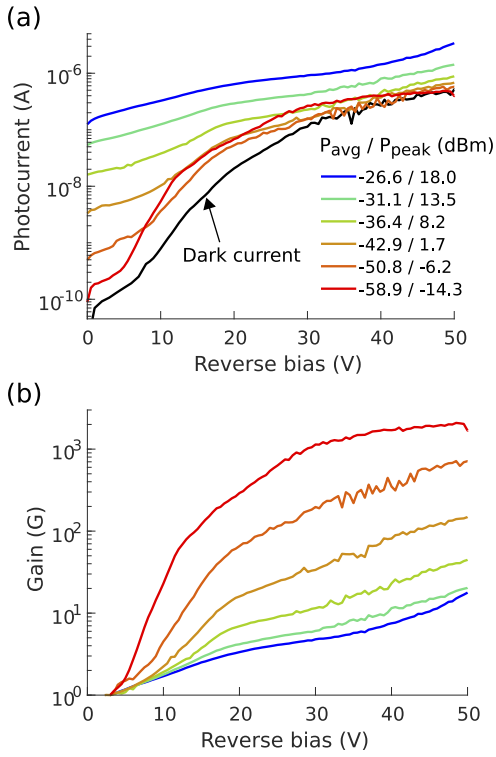

Fig. 5. (a) Current–voltage measurements at different optical input powers and (b) corresponding avalanche gain. A picosecond laser at 775 nm was used as an optical source. The dark current measured without illumination is also shown in (a), reaching 107 pA at 3 V. The reverse bias voltage was swept until 50 V, sufficiently below the observed breakdown voltage $V_{br} \approx 80$ V.

remove the native oxide, reducing the metal–semiconductor contact resistance. A micrograph of the post-processed Si p–i–n photodetector on the silicon nitride waveguide is shown in Fig. 3(b).

Results. The photodetector was characterized at room temperature using electrical contact probes and a Keithley 2400A voltage–current source. The optical input was provided using a silicon nitride grating coupler and a cleaved fiber. A polarization controller was used to couple in TE-polarized light. From the *V–I* measurements, it was found that the differential resistance converges to a value of 40 Ω. Furthermore, a dark current of 107 pA was measured at a reverse bias voltage of 3 V. This dark current is low compared with most state-of-the-art integrated photodetectors [15,18,21,22] and comparable to the results in Ref. [16]. The waveguide-referred responsivity, defined with respect to the power in the SiN waveguide, was measured at 800 nm and 775 nm. A Ti:sapphire continuous wave laser (M2 SolsTis) was used for characterization at 800 nm, whereas a Onefive Katana picosecond laser was used for measurements at 775 nm. The responsivity and corresponding external quantum efficiency as a function of reverse bias voltage are depicted in Fig. 4(a). Losses from the grating couplers are not taken into account.

Similar responsivities around 0.19 A/W and external quantum efficiencies around 30% at −3 V bias voltage were obtained for both wavelengths. The responsivity was also simulated using Lumerical's FDTD and CHARGE simulators by calibrating the recombination parameters to match simulated and measured dark currents. The resulting simulated responsivity is approximately 14% higher than the experimental results. This discrepancy can probably be attributed to overestimation of the optical input power and some uncertainty in the model's recombination parameters. Furthermore, simulations show a ~2% reduction in responsivity for a lateral misalignment of 1 μm, demonstrating robustness against alignment offsets of the microtransfer printing process.

To estimate the photodetector bandwidth, its impulse response was captured using a Teledyne Lecroy 65 GHz real-time oscilloscope (RTO) and a Onefive Katana picosecond laser. The latter generates optical pulses with a duration around 35 ps. The Keithley current–voltage source and RTO were connected to the high-speed radio frequency (RF) probe using a bias tee. A full width at half maximum around 91 ps was obtained for reverse bias voltages in excess of −1.5 V, as depicted in Fig. 4(b). From this, the 3 dB bandwidth can be estimated by Fourier transforming the measured impulse response and dividing it by the Fourier transform of the time-domain optical picosecond pulse trace, which is provided in the Onefive Katana laser output specification sheet. This derivation yields a 3 dB bandwidth of 6 GHz, a value that is mainly limited by the *RC* time delay as S_{11} measurements indicate that the resistance and photodiode capacitance at 3 V reverse bias are approximately 183 Ω and 133 fF, respectively.

For applications where high receiver sensitivities are indispensable, on-chip avalanche photodiodes (APDs) with an internal multiplication gain offer an attractive solution [22]. As silicon exhibits a low impact ionization ratio and consequently limited excess noise, Si-based APDs are particularly

suited for avalanche detection [19]. To investigate the avalanche capabilities of the microtransfer printed Si p–i–n photodiode, the current–voltage relation was measured for reverse bias voltages up to 50 V, below the breakdown voltage $V_{br} \approx 80$ V. The I–V measurement was carried out with different optical input powers at 775 nm, as shown in Fig. 5(a). The specified power values take into account the grating coupler losses and hence represent the optical power in the SiN waveguide. The avalanche gain $G(V_B)$, shown in Fig. 5(b), can be calculated as the ratio of the photocurrent at a given reverse bias voltage V_B divided by the photocurrent at the unity gain point. The latter is here defined as the point where the second derivative of the photocurrent with respect to bias crosses zero (here at $V_B \approx 3$ V), in correspondance with Ref. [16]. The highest observed gain–bandwidth product is 68 GHz at 45 V reverse bias for an optical input power of $P_{opt} \approx -26$ dBm. From Fig. 5(b), it is obvious that the observed avalanche gain is higher for lower optical input powers. This can be expected as more charge carriers are generated at higher optical input powers, leading to an enhanced space charge effect and consequently saturation of the photocurrent [16]. Moreover, as a picosecond laser source was used as an input, this saturation effect is more pronounced. Although the photodiode reverse bias voltage was here swept until 50 V, typical CMOS platforms only supply voltages up to 12 V [19]. At this bias point, avalanche gains up to ~60 are observed for low optical input powers. Photodiodes with a narrower intrinsic region or an interdigitated structure could be used to reduce the breakdown voltage and boost the avalanche gain at lower bias voltages, although this typically comes at the expense of an increased dark current [16].

Discussion. We have successfully demonstrated, to our knowledge, the first microtransfer printed Si photodiodes, based on imec's iSiPP25G integrated silicon photonics platform, on a generic commercially available SiN platform for wavelengths below 850 nm. This heterogeneous integration approach offers full CMOS compatibility and enables wafer-scale manufacturing. Furthermore, a novel process flow for microtransfer printing was developed based on a release etch with HF vapor. In contrast with liquid release etchants, a vapor-phase release etch provides a near 100% picking yield as it does not suffer from capillary forces that can lead to a collapse of the suspended Si layer. Four photodiodes were fabricated and measured with no discernible differences, confirming the potential of the fabrication process. Our devices feature competitive performance with a low dark current of 107 pA at 3 V reverse bias, external quantum efficiencies around 30% at 775 nm and 800 nm, and a 3 dB bandwidth of 6 GHz. In addition, avalanche gain was demonstrated to serve applications where higher receiver sensitivities are needed. These results showcase that our heterogeneously integrated photodiodes can conveniently extend the scope of commercial SiN platforms to serve applications beyond the telecom domain, such as biosensing, imaging, and quantum photonics.

Funding. Fonds Wetenschappelijk Onderzoek (11F8120N, 12ZB520N); Bijzonder Onderzoeksfonds UGent; European Research Council (Starting grant ELECTRIC).

Acknowledgments. The authors thank S. Verstuyft for help with the photodetector processing and G. Ong for his contributions to the simulations.

Disclosures. The authors declare no conflicts of interest.

Data availability. Data underlying the results presented in this paper are not publicly available at this time but may be obtained from the authors upon reasonable request.

REFERENCES

1. A. Rahim, E. Ryckeboer, A. Z. Subramanian, S. Clemmen, B. Kuyken, A. Dhakal, A. Raza, A. Hermans, M. Muneeb, S. Dhoore, Y. Li, U. Dave, P. Bienstman, N. Le Thomas, G. Roelkens, D. Van Thourhout, P. Helin, S. Severi, X. Rottenberg, and R. Baets, J. Lightwave Technol. **35**, 639 (2017).
2. D. J. Blumenthal, R. Heideman, D. Geuzebroek, A. Leinse, and C. Roeloffzen, Proc. IEEE **106**, 2209 (2018).
3. P. Marin-Palomo, J. N. Kemal, M. Karpov, A. Kordts, J. Pfeifle, M. H. P. Pfeiffer, P. Trocha, S. Wolf, V. Brasch, M. H. Anderson, R. Rosenberger, K. Vijayan, W. Freude, T. J. Kippenberg, and C. Koos, Nature **546**, 274 (2017).
4. B. Shen, L. Chang, J. Liu, H. Wang, Q.-F. Yang, C. Xiang, R. N. Wang, J. He, T. Liu, W. Xie, J. Guo, D. Kinghorn, L. Wu, Q.-X. Ji, T. J. Kippenberg, K. Vahala, and J. E. Bowers, Nature **582**, 365 (2020).
5. S. Cuyvers, B. Haq, C. Op de Beeck, S. Poelman, A. Hermans, Z. Wang, A. Gocalinska, E. Pelucchi, B. Corbett, G. Roelkens, K. Van Gasse, and B. Kuyken, Laser Photonics Rev. **15**, 2000485 (2021).
6. J. M. Arrazola, V. Bergholm, K. Brádler, T. R. Bromley, M. J. Collins, I. Dhand, A. Fumagalli, T. Gerrits, A. Goussev, L. G. Helt, J. Hundal, T. Isacsson, R. B. Israel, J. Izaac, S. Jahangiri, R. Janik, N. Killoran, S. P. Kumar, J. Lavoie, A. E. Lita, D. H. Mahler, M. Menotti, B. Morrison, S. W. Nam, L. Neuhaus, H. Y. Qi, N. Quesada, A. Repingon, K. K. Sabapathy, M. Schuld, D. Su, J. Swinarton, A. Száva, K. Tan, P. Tan, V. D. Vaidya, Z. Vernon, Z. Zabaneh, and Y. Zhang, Nature **591**, 54 (2021).
7. C. Bruschini, H. Homulle, I. M. Antolovic, S. Burri, and E. Charbon, Light: Sci. Appl. **8**, 87 (2019).
8. M. A. Porcel, A. Hinojosa, H. Jans, A. Stassen, J. Goyvaerts, D. Geuzebroek, M. Geiselmann, C. Dominguez, and I. Artundo, Opt. Laser Technol. **112**, 299 (2019).
9. H. Zhao, S. Clemmen, A. Raza, and R. Baets, Opt. Lett. **43**, 1403 (2018).
10. C. Xiang, W. Jin, J. Guo, J. D. Peters, M. J. Kennedy, J. Selvidge, P. A. Morton, and J. E. Bowers, Optica **7**, 20 (2020).
11. C. O. de Beeck, B. Haq, L. Elsinger, A. Gocalinska, E. Pelucchi, B. Corbett, G. Roelkens, and B. Kuyken, Optica **7**, 386 (2020).
12. J. Goyvaerts, S. Kumari, S. Uvin, J. Zhang, R. Baets, A. Gocalinska, E. Pelucchi, B. Corbett, and G. Roelkens, Opt. Express **28**, 21275 (2020).
13. Y. Fan, A. van Rees, P. J. M. van der Slot, J. Mak, R. M. Oldenbeuving, M. Hoekman, D. Geskus, C. G. H. Roeloffzen, and K.-J. Boller, Opt. Express **28**, 21713 (2020).
14. X. Hu, D. Wu, H. Zhang, W. Li, D. Chen, L. Wang, X. Xiao, and S. Yu, Photonics Res. **9**, 749 (2021).
15. A. Chatterjee, Saumitra, S. K. Sikdar, and S. K. Selvaraja, Opt. Lett. **44**, 1682 (2019).
16. S. Yanikgonul, V. Leong, J. R. Ong, T. Hu, S. Y. Siew, C. E. Png, and L. Krivitsky, Nat. Commun. **12**, 1834 (2021).
17. M. Bernard, F. Acerbi, G. Paternoster, G. Piccoli, L. Gemma, D. Brunelli, A. Gola, G. Pucker, L. Pancheri, and M. Ghulinyan, Optica **8**, 1363 (2021).
18. Q. Yu, J. Gao, N. Ye, B. Chen, K. Sun, L. Xie, K. Srinivasan, M. Zervas, G. Navickaite, M. Geiselmann, and A. Beling, Opt. Express **28**, 14824 (2020).
19. Z. Huang, C. Li, D. Liang, K. Yu, C. Santori, M. Fiorentino, W. Sorin, S. Palermo, and R. G. Beausoleil, Optica **3**, 793 (2016).
20. L. Hoffman, A. Subramanian, P. Helin, B. Du Bois, R. Baets, P. Van Dorpe, G. Gielen, R. Puers, and D. Braeken, IEEE Photonics J. **8**, 1 (2016).
21. B. Wang, Z. Huang, Y. Yuan, D. Liang, X. Zeng, M. Fiorentino, and R. G. Beausoleil, Photonics Res. **8**, 1118 (2020).
22. L. Virot, P. Crozat, J.-M. Fédéli, J.-M. Hartmann, D. Marris-Morini, E. Cassan, F. Boeuf, and L. Vivien, Nat. Commun. **5**, 4957 (2014).